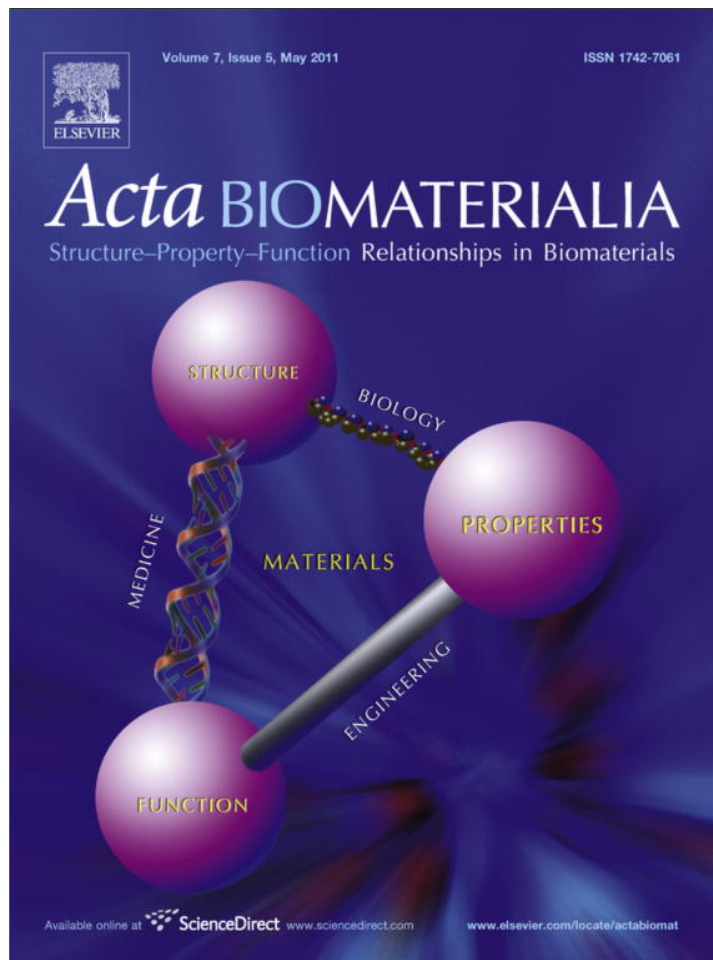


Provided for non-commercial research and education use.
Not for reproduction, distribution or commercial use.



This article appeared in a journal published by Elsevier. The attached copy is furnished to the author for internal non-commercial research and education use, including for instruction at the authors institution and sharing with colleagues.

Other uses, including reproduction and distribution, or selling or licensing copies, or posting to personal, institutional or third party websites are prohibited.

In most cases authors are permitted to post their version of the article (e.g. in Word or Tex form) to their personal website or institutional repository. Authors requiring further information regarding Elsevier's archiving and manuscript policies are encouraged to visit:

<http://www.elsevier.com/copyright>



Contents lists available at ScienceDirect

Acta Biomaterialia

journal homepage: www.elsevier.com/locate/actabiomat

Interdigitating biocalcite dendrites form a 3-D jigsaw structure in brachiopod shells

Andreas J. Goetz^{a,*}, David R. Steinmetz^b, Erika Griesshaber^a, Stefan Zaefferer^b, Dierk Raabe^b, Klemens Kelm^c, Stephan Irsen^d, Angelika Sehrbrock^d, Wolfgang W. Schmahl^a

^a Department für Geo- und Umweltwissenschaften, LMU, Theresienstr. 41, D-80333 München, Germany

^b Max-Planck-Institut für Eisenforschung, Max-Planck-Straße 1, D-40237 Düsseldorf, Germany

^c German Aerospace Center (DLR), Institute for Materials Research, Linder Höhe, D-51147 Köln, Germany

^d Forschungszentrum CAESAR, Ludwig-Erhard-Alle 2, D-53175 Bonn, Germany

ARTICLE INFO

Article history:

Received 7 October 2010

Received in revised form 21 January 2011

Accepted 26 January 2011

Available online 2 February 2011

Keywords:

High-resolution EBSD

Brachiopod primary layer texture

Interdigitated/interlinked dendritic microstructure

Hybrid composite biomaterial

Nacre

ABSTRACT

We report a newly discovered dense microstructure of dendrite-like biocalcite that is formed by marine organisms. High spatial resolution electron backscatter diffraction (EBSD) was carried out under specific analytical conditions (15 and 10 kV) on the primary layer of the modern brachiopod *Gryphus vitreus*. The primary layer of modern brachiopods, previously termed nanocrystalline, is formed by an array of concave/convex calcite grains with interdigitated recesses and protrusions of abutting crystals without any cavities in or between the dendrites. The interface topology of this structure ranges from a few tens of nanometres to tens of micrometres, giving a nanoscale structure to the material fabric. The dendritic grains show a spread of crystallographic orientation of several degrees and can thus be referred to as mesocrystals. Individual dendritic mesocrystals reach sizes in one dimension larger than 20 μm . The preferred crystallographic orientation is similar in the primary and adjacent fibrous shell layers, even though these two layers show completely different crystal morphologies and grain boundary topologies. This observation indicates that two separate control mechanisms are active when the primary and the fibrous shell layers are formed. We propose a growth model for the interdigitated dendritic calcite grain structure based on a precursor of vesicles filled with amorphous calcium carbonate (ACC).

© 2011 Acta Materialia Inc. Published by Elsevier Ltd. All rights reserved.

1. Introduction

Mineralized structures generated by biological control are widely recognized in material science and nanotechnology as prototypes for advanced materials. Regardless of whether they are carbonate-, phosphate- or silica-based, they are hybrid composites with complex structures on several hierarchical levels (e.g. [1–3]). Within the hierarchical organization, each level contributes to the overall function of the biomaterial and thus influences the properties and shape of the final product (e.g. [2,4–6]). Thus, the investigation of biological hard tissues may not only provide pathways for the development and production of tougher materials, notably in the low-energy/cost sector, but also new materials for extreme performance requirements.

Brachiopods are marine invertebrates that exist since the early Cambrian (e.g. [7,8]). They live in a wide range of marine habitats and mineralize either low-Mg (<5 wt.% Mg) calcite (the *Rhynchonelliformea* and *Craniiformea*) or Ca-phosphate (the *Linguliformea*) shells [9]. Their formation of two different types of shell chemistry (carbonate and phosphate) with distinct shell design strategies makes them interesting candidates for understanding

biomineralization processes and material properties of exoskeleton biomaterials employed in marine habitats [10–16]. In brachiopod and bivalve shells the hierarchical design of the composite material is of profound importance to the shell's mechanical properties [10,12,15–19]. For example, as the scale of the microstructure decreases, the weakening influences of defects become less important [20]. Thus, the small-scale composite structure and a hierarchical architecture are intrinsic features of all biomaterials [3]. Therefore, a complete and thorough understanding of the different parameters involved in the construction of biomaterials is essential for the biomimetic development of advanced engineering materials [21].

Calcitic brachiopod shells are multi-layered on the submillimetre scale (Fig. 1). The majority of modern calcitic brachiopods synthesize two-layered shells, with a thin, fine-grained (nano- to microscale) “primary” outer layer with a thickness of 0.05–0.1 mm and a coarser grained, fibrous “secondary” inner layer with a thickness of 0.5–1 mm (e.g. [7,8,12]). Some brachiopod species build three-layered shells composed of a primary layer, a fibrous layer and a columnar layer [10], as is the case for the investigated species *Gryphus vitreus*. The fibres and the columns are calcite single crystals within the precision of electron backscatter diffraction (EBSD), i.e. ~ 0.1 – 0.5° . We observed lengths of these crystals up to 1 mm. Cross-sections are of the order of 5–15 μm for fibres and

* Corresponding author. Tel.: +49 89 2180 4314.

E-mail address: andreas.goetz@lrz.uni-muenchen.de (A.J. Goetz).

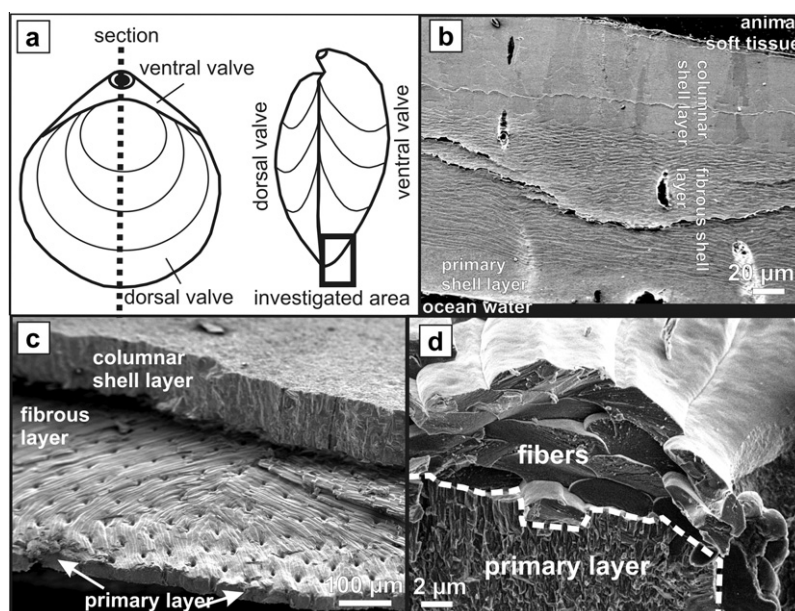


Fig. 1. (a) Generic sketch of the shape of the brachiopod valves. The black rectangle in the centre image indicates the area that has been investigated in this study. (b) SEM image (SE contrast) of the investigated EBSD sample. It was taken in the same sample orientation as the EBSD maps: the soft tissue of the animal was located next to the valve in the upper part of the image, while the outer border of the primary shell layer gives the shell portion that was in contact with sea water. (c) SEM image (SE contrast) of the fractured surface of a brachiopod shell, showing all three (columnar, fibrous and primary) layers. (d) A further magnification of the primary and fibrous layers (SE contrast). Single fibres of the fibrous layer can be easily distinguished, whereas the primary layer has a rough and grainy fracture surface.

20–100 μm for the columns, respectively. The crystals are separated by intercrystalline biopolymer layers [12,15,16,22]. They also contain nanoscale biopolymers within the crystals [15]. It is likely that the calcite is produced from an amorphous precursor [23], which has been described for many biomaterials [24–26].

In the coarse microstructure, the crystallographic texture plays a major role in improving the shell's mechanical strength [10,12,15,16,27]. Textural properties were determined by EBSD analyses. An accelerating voltage of 20 kV was used in previous studies and a typical spatial resolution of 1 μm was obtained. This resolution served to obtain a rough estimate of the general crystallographic texture of the primary layer [15,28], but failed to resolve corresponding texture data at the nanoscopic scale of the structure. Steinmetz et al. [29] have recently significantly improved the spatial EBSD resolution by applying lower accelerating voltages. The decrease in accelerating voltage leads to a smaller interaction volume and thus to a better spatial resolution [30]. By using this technique, our aim in this study was to resolve the nanometre-sized crystals of the brachiopod primary layer in order to obtain a deeper insight into the texture and microstructure, and thus a better understanding of the synthesis and the properties of this material. To achieve these objectives, we chose to analyze the primary layer of the calcitic, three-layered brachiopod species *G. vitreus* that has recently been investigated microchemically and mechanically in great detail [31].

2. Samples and methods

The investigated sample was a specimen of the dorsal valve of the modern brachiopod *G. vitreus* (Born). The shell was sectioned along its median plane (Fig. 1) and 200 μm thick shell wafers were cut out. A highly smooth surface of the shell wafer was prepared by first polishing the section with diamond paste (0.25 μm particle size) and subsequently attack-polishing the sample with a suspension of alumina nanoparticles. The samples were then cleaned, dried and coated with the thinnest possible conducting carbon coating.

High-resolution EBSD patterns were collected on a Zeiss 1540 XB dual-beam focused ion beam (FIB) field-emission scanning electron microscope (SEM) with an EDAX/TSL EBSD system (TSL OIM Data Collection software version 5.31). The accelerating voltages used in the experiments were 15 and 10 kV, respectively. The aperture used was 30 μm , the beam currents were 490 pA at 15 kV and 390 pA at 10 kV, and the spot size was under 5 nm. The sample was tilted 70° towards the detector, resulting in an angle of 20° between the electron beam and the sample surface. Although the pattern quality was significantly better for 15 kV, the use of an accelerating voltage of 10 kV also gave indexable Kikuchi patterns with good confidence indices. The step sizes used were between 0.05 and 0.15 μm . For both accelerating voltages 40–60% of the obtained Kikuchi patterns could be indexed crystallographically. The average diffraction pattern quality (PQ; [32]) of the indexed patterns was 2200–2400 for 15 kV and 1500 for 10 kV, respectively. All orientation data were processed with confidence index standardization and grain dilation single iteration procedures. For the data shown in Fig. 4, the grain dilation iteration was performed twice, while for the data sets shown in Fig. 5 it was performed only once. Details of the orientation of the sample are shown in Fig. 1. SEM images of the samples were taken using a field emission gun SEM JEOL JSM 6500 F electron microscope in which the samples were tilted 23°, resulting in an angle of 77° between the sample surface and the electron beam. All images were collected with a secondary electron (SE) detector. However, even though the contrast formed by the SE detectors is dominated by secondary electrons, backscatter electrons (BSE) also exert an influence on the contrast [33]. As the thin section investigated is very flat, the images are sometimes influenced by BSE contrast.

Both FIB sectioning and TEM imaging was performed at Forschungszentrum Caesar, Bonn, Germany. TEM imaging was performed on FIB-prepared samples. FIB lamellae were cut 90° to the surface mapped by EBSD. The FIB lamellae were obtained on a LEO XB1540 FIB workstation with a combination of high-resolution SEM and a GEMINI field-emission column. Ion milling was performed with Ga ions at 30 keV. The beam was tilted 1.3°

to the 90° milling direction to compensate for the convergence of the beam. For final milling, a probe current of 10 pA was applied.

TEM imaging was done on a corrected illumination scanning probe Zeiss Libra 200 transmission electron microscope (TEM). The instrument is equipped with a Schottky field-emission gun, a monochromator for the electron beam, a Cs corrector for the illumination system and several imaging energy filters for the production of energy-selective TEM images. In order to optimize the diffraction contrast, the samples were tilted near a zone axis. TEM images were taken with a large objective aperture.

3. Results

3.1. SEM and TEM observations

In the SEM images of fractured surfaces (Fig. 1d), the primary layer appears bulky and shows a rough surface. On the thin section electron micrographs (Fig. 2a and b), the primary layer is seen to consist of an array of interdigitated calcite grains. The cross-sections of the grains are elongated, showing lengths of 2–6 μm and widths of 0.5–1.5 μm . The elongation direction is always perpendicular to the surface of the shell. The morphology of individual grains shows concave recesses reminiscent of skeletal or dendritic crystals. Neighbouring grains have mutually grown into the recess zones of the abutting crystals, forming a dense microstructure of interlocked crystals. These microstructural features can also be found after measurements of an EBSD map. Within the grain

boundaries, organic molecules are destroyed by the electron beam. The remains are non-conductive and show a brighter contrast in SE images (Fig. 2c). This specific structure is also visible from the EBSD maps (see Sections 3 and 4 below).

The TEM micrographs in Fig. 3 highlight the internal structure of the primary shell layer in more detail. TEM images were obtained on FIB-prepared samples. On the micrometre scale (Fig. 3a) we find several grains exhibiting pseudotopographic phase contrast at their boundaries due to varying focus conditions caused by sample bending. The boundaries in Fig. 3a are imaged through a slight defocusing of the TEM.

Fig. 3b and c show the boundary between two differently oriented grains within the primary shell layer. While the grain on the left-hand side of Fig. 3b shows intense phase contrast effects, most probably because it is oriented near a low indexed zone axis, the contrast in the crystal on the right-hand side is dominated by absorption contrast. Here, small somatoid (cigar-shaped) areas of lower density are observed. These areas are unlikely to be produced by beam damage during the investigation, as their appearance did not change during the TEM investigation. Fig. 3c contains the boundary in Fig. 3b at higher magnification. Besides the somatoid areas of lower density, the linear boundaries are the most prominent feature. The area is correctly focused, as indicated by the lattice fringes visible in the centre of Fig. 3c, while the linear structures show a finite width of about 1 nm. In analogy to the organic membranes separating the fibrous crystals in brachiopod shell secondary layers [23], we assume a thin organic membrane to be present between two grains.

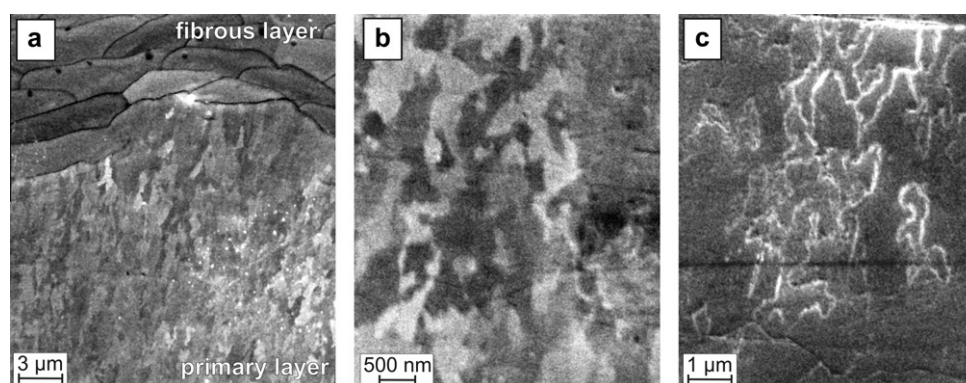


Fig. 2. SEM micrographs of the investigated shell section of the modern brachiopod *G. vitreus*. The top part of (a) shows the fibrous shell layer while the lower part gives a detailed image of the microstructure of the primary layer (BSE and SE contrast are present). (b) A higher-magnification image of the primary shell layer. Clearly visible interdigitating grains form a nanoscale array of grain boundaries, forming a jigsaw-like composite (BSE contrast). (c) Image of the primary layer after an EBSD map has been measured on that shell portion. Grain boundaries are clearly visible (SE contrast).

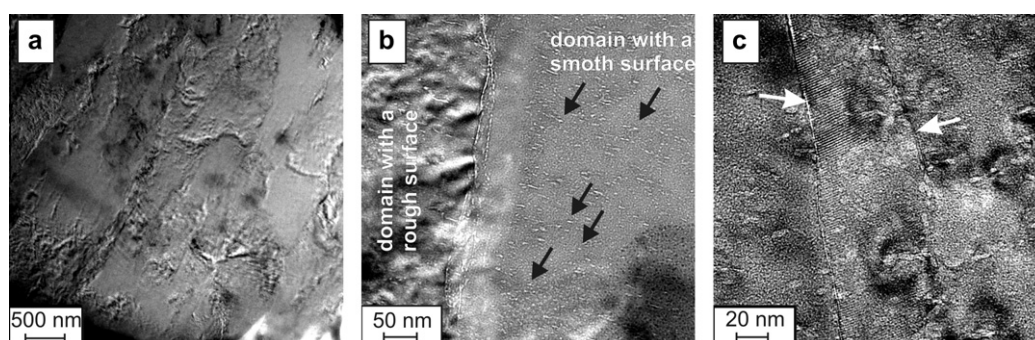


Fig. 3. TEM bright field images taken on an FIB lamella cut out from the primary layer of *G. vitreus*. In (a) several differently sized grains can be observed. The image has been defocused to highlight the discontinuity at the grain boundaries of neighbouring crystallites. (b) Two abutting grains. Areas of lower density appear as white spots and some are marked with black arrows. (c) A thin (0.5–1.5 nm), presumably organic, membrane is visible at the boundary between the two grains shown in (b).

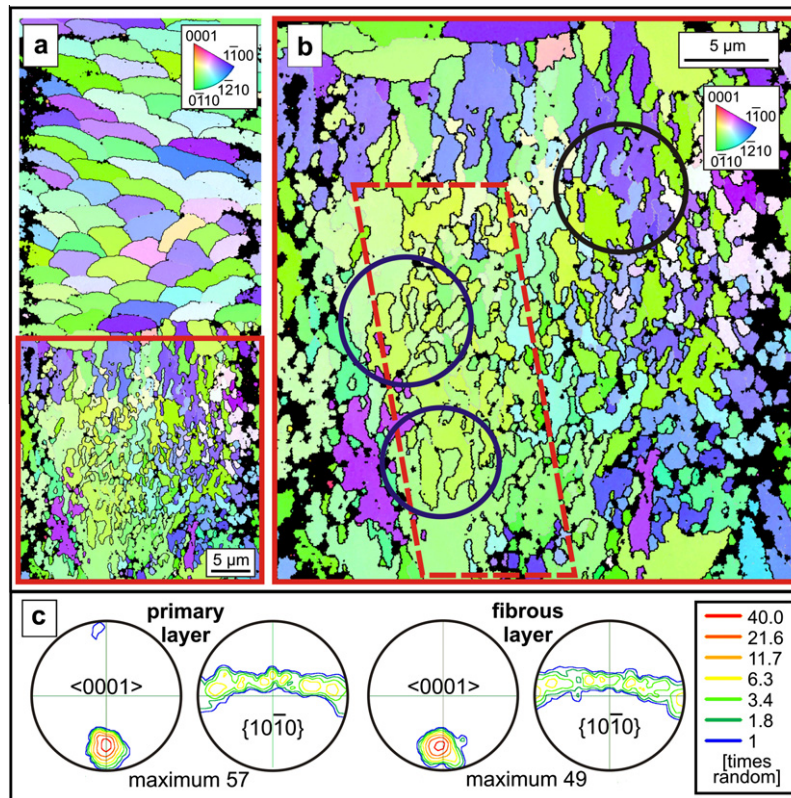


Fig. 4. High-resolution EBSD map of the primary and the fibrous shell layers of the modern brachiopod *G. vitreus*. EBSD maps are coloured in an inverse pole figure colour scheme. The black regions in (a and b) correspond to measured points, with a confidence index of <math><0.1</math>. Small-angle grain boundaries are marked with grey lines, grain boundaries with black lines. In the upper part of the map of (a) a cross-section through the fibrous secondary shell layer is shown. In the lower part of the figure the primary shell layer, with its micro-/nanoscale fabric, is presented. (b) Higher-magnification image of the red rectangle in (a). Examples of strongly splined and interlocked grains in the interdigitated jigsaw microstructure of the primary layer are highlighted: the blue circles indicate prominent examples of interdigitating grains, while the black circle emphasizes grains which are almost completely embedded in another grain. The red parallelogram outlines a shell portion which is composed of only two dominant grain orientations (or grains) that form a section through the interface of two distinct dendritic crystals. (c) The recalculated pole figures of the texture of the primary layer and the fibrous shell layer. A sharp (0 0 0 1) fibre texture for both layers is observed. The probability density is indicated in “times random” multiples.

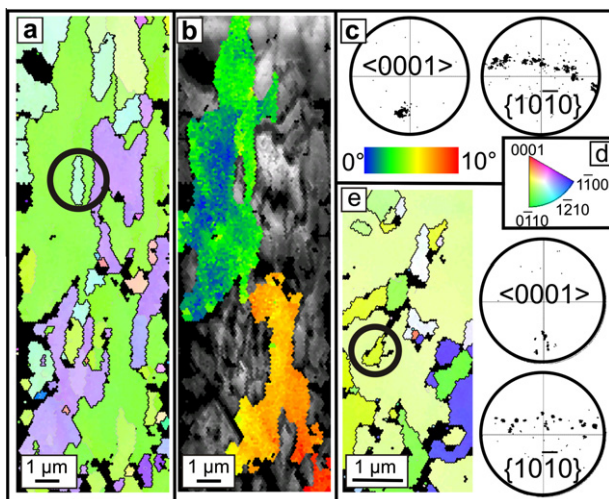


Fig. 5. EBSD maps and corresponding pole figures of the primary layer of *G. vitreus*. Grain orientations (a) are displayed by the inverse pole figure colour scheme in (d). Note that the entire map is dominated by only one grain (appearing in green). The black circle marks an example of a crystal that is entirely surrounded by another grain. (b) The same EBSD data set as in (a) with diffraction PQ shown in greyscale and the internal mesocrystal mosaicity of the dominant grain highlighted in rainbow-colours coding for the a^* -axis orientation with respect to a continuous colour scale covering 10° (c). The EBSD map of (e) is dominated by a single large grain appearing in very light green; the variations in green shades show the internal mosaicity. Pole figures that correspond to the EBSD maps of (a), (b) and (e) are given in (c) and adjacent to (e), respectively.

3.2. EBSD mapping of microstructure and texture

Figs. 4 and 5 show EBSD measurements on the primary and the fibrous shell layers of *G. vitreus* measured at 15 kV (Figs. 4 and 5a and b) and 10 kV (Fig. 5e). The largest EBSD map analysed in this study (Fig. 4a and b) covers a shell portion with both the primary and the fibrous shell layer. The crystallographic and microstructural aspects of the coarse-grained fibrous layer have been described in detail in previous studies on other brachiopod species (*Megerlia truncata* [16], *M. truncata*, *Terebratalia transversa* [12,15], *Liothyrella neozelanica*, *L. uva* [10]), and *G. vitreus* forms no exception.

In the EBSD maps, individual grains appear as areas of uniform colour. In the present paper we use the continuity argument to define a grain: directly neighbouring measurement points in EBSD maps that have the same crystallographic orientation within $\pm 3^\circ$ belong to one grain. Misorientation in the range of 3–15° between two different grains is marked with grey lines (small angle grain boundaries), while above 15° they are marked with black lines (grain boundaries). In EBSD maps of the fine-grained (earlier referred to as nanocrystalline, e.g. [10]) primary layer these grains comprise elongated concave/convex shapes with multiple recesses and protrusions which sometimes have dimensions like the bulk grain interior. These shapes are also observable from the orientation-contrast in the SEM images of Fig. 2 and the TEM images of Fig. 3. Thus the individual grains of the primary layer resemble dendritic structures. However, unlike dendrites, these grains form a dense interdigitating microstructure (Figs. 4b, 5a and b, 6c and d)

where grain diameters between 500 nm and 5 μm prevail. Occasionally we even observe grains longer than 20 μm (e.g. in the map shown in Fig. 5a and b).

As indicated by the dashed red parallelogram in Fig. 4b, often only two distinct grain orientations (here shown by light green and yellowish green colours) are present in large portions of the EBSD map. In Figs. 4b (black circle), 5a (black circle) and 5e (black circle) shell portions are highlighted where the cross-section of one grain (area of uniform colour) is completely surrounded by another grain (i.e. another area of uniform colour). The crystallographic orientation of the grains in the primary layer is such that calcite c -axes $[0001]$ (parallel to the (0001) pole in the trigonal system) are perpendicular to the surface of the shell. No preferred orientation of the a^* -axes $\{10\bar{1}0\}$ is present; however, neighbouring grains are always rotated by at least 15° (indicated by black grain boundaries) relative to each other around their c -axes. Thus, the preferred crystallographic orientation of the primary layer is a $[0001]$ fibre texture with (0001) plane normals perpendicular to the shell surface. Pole figures of the crystals of the fibrous layer and of the interlocked crystals of the primary layer (Fig. 4g and h) show essentially the same (0001) fibre texture, with the c -axis parallel to the radius of the curvature of the shell. The maximum of the (0001) pole figures is 57 times random for the primary layer and 49 times random for the secondary layer. These observations underline the strong similarity in the textures of both layers even though their microstructures are extremely different (Fig. 4c).

4. Discussion

In the present study, the EBSD step size and spatial resolution, area of coverage, diffraction resolution and grain statistics have been much improved and are now sufficient to interpret the primary layer structure in a more consistent manner. One major observation of the present study is that we obtain similar orientation distributions functions for the primary and secondary shell layers even though they have fundamentally different grain morphologies and grain boundary topologies (see Fig. 4a and c). From the conspicuous microstructure of the columnar layer of the shell of *L. neozelanicus* [10] we concluded that the axial texture of the preferred crystallographic orientation in brachiopod shells is caused by competitive growth starting from nuclei with a random orientation distribution. The similar texture of the primary layer and the fibrous layer presented in this study shows that this model is probably not valid. It appears that nucleation already occurs with a well-defined orientation with respect to the entire skeleton. This probably takes place in the same way for all brachiopod shell layer microstructures: the interdigitated (primary), the fibrous and the columnar shell layers.

The definition that we use here to define a grain (directly neighbouring measurement points in EBSD datasets that have the same crystallographic orientation within $\pm 3^\circ$ belong to one grain) allows a situation where a grain gradually changes its orientation over its length: in the investigated samples for up to 10° within one grain (compare Fig. 5a and b). The change in orientation within individual grains indicates that these crystals represent mesocrystals, i.e. they are highly ordered aggregates consisting of nanoparticles that assemble in good but not perfect crystallographic register [34]. Mesocrystalline arrangements are commonly observed in calcitic biomaterials [35,36]. The present study reveals that the primary layer microstructure of *G. vitreus* consists of a complex assembly of micrometre-sized three-dimensionally interdigitating grains. Apart from the direct spatial and crystallographic observation of interlocking recesses and protrusions among abutting crystals, we observe several occasions where areas with similar orientation are separated by a grain of different orientation. We assume that

these similarly orientated areas belong to the same grain, and that we look at the interface structure of two interdigitated grains (see the shell portion within the white parallelogram in Fig. 4b). This observation also means that we can identify grains within the primary shell layer of this brachiopod species that are larger than 20 μm (such as the large grain shown in Fig. 5a and b). Accordingly, the “grain size” of the formerly discussed “nanocrystalline primary layer” is not simply nanoscaled, as it has hitherto been described. In two-dimensional images this interlocked microstructure can lead to an incorrect interpretation of the average grain size. Moreover, as for dendritic crystals, the common term “grain size” needs to be differentiated into the width of cross-sectioned branches of the dendrite and the extension of the complete dendrite with coherent crystallographic orientation of all its branches. The present study shows that the skeletal calcite mesocrystals of the brachiopod primary layer reach lengths of several tens of micrometres. The nanoscale feature of the primary layer is rather the distance between interfaces of abutting interdigitated crystals. The interlocking grains of the brachiopod shell primary layer as observed in the present study is in concert with the TEM observations on the primary layer of the terebratulide brachiopod *M. truncata* [23], where image series taken at different specimen tilts highlight the nanoscale cross-sections of the individual crystallites together with their interdigitating boundaries.

The newly discovered microstructure also resolves the question why the primary layer is twice as hard as the secondary layer in microindentation [12,15], while both layers have the same hardness in nanoindentation [15,27]. The nanoscale indents simply probe individual crystals of calcite, while microindents probe the microstructure.

From our EBSD data sets we can identify two major mechanisms for mechanical optimization of the primary layer material:

- a) Crack deflection and crack splitting within the biocalcite crystallites is improved by the mesocrystalline assemblage (possibly involving intracrystalline macromolecules [15]) – a mechanism common in biominerals (e.g. [20]).
- b) The jigsaw topology of the polycrystalline assembly:
 - distributes the stress at a crack tip over a large volume and leads a crack into a labyrinth lowering the chance of catastrophic failure; and
 - increases the abrasion resistivity of the primary layer: a simple fracture through one grain cannot remove the grain from the microstructure. Note that the primary layer is the outer mineralized layer.

We are not aware of any inorganic microstructure that shows such a strong interdigitation of crystals. The primary layer calcite crystals resemble dendrites. In dendritic alloy solidification, for example, there are no structures with a similarly dense interdigitation of crystals as observed here. Eutectic and eutectoid microstructures also show grain interlocking somewhat similar to those found in this study [37–40], but these are either multi-phase aggregates [39] or do not show an interlocking microstructure of crystals of the same phase [38]. Interdigitated microstructures are extremely favourable for the mechanical behaviour of ceramic-like compounds [41]. Microstructures with a smaller degree of interlocking than observed in this study already proved their resistivity in SiC ceramics in Ref. [42], where it was shown that the interlocking of elongated grains can dramatically improve the sliding wear resistance of the ceramic material.

We observed crystallization phenomena on two length scales: (i) the formation of mesocrystals (mosaic crystals) composed of nanoscale units [34] and (ii) the formation of the three-dimensional (3-D) jigsaw structure of interdigitating microscale mesocrystals.

We can envisage two possible mechanisms to produce this interdigitating structure. The first is to build an organic precursor structure pre-defining the dendrite-like shapes with membranes and to subsequently mineralize the caverns between the membranes. The second and more likely mechanism, which also explains the formation of mesocrystals at the same time, is sketched in Fig. 6: nanosized capsules (Fig. 6a) filled with amorphous calcium carbonate (ACC) and surrounded by delicate vesicle membranes are assembled (Fig. 6a) and the ACC crystallizes within the capsules, starting from calcite nucleation sites. Indeed, Griesshaber et al. [23] observed the crystallization of an ACC fibre in secondary layer brachiopod shell material in situ in a TEM. The ACC capsules are formed as vesicles inside the epithelial cells and are then moved to the primary layer by exocytosis, according to an observation of Williams [43]. The crystallization of calcite from ACC proceeds from one capsule to the next. Mineral bridges [44,45] punctuating the vesicle membranes are able to carry the information on crystallographic orientation from one capsule to the next. The mineral bridges may form by disruption of the membranes, e.g. induced by forces of crystallization (Fig. 6a). In consequence, numerous capsules, connected by continuous pathways of crystallization through mineral bridges, form one calcite grain.

The crystallization process from ACC will induce stresses due to at least three reasons: volume and/or shape change, accumulation of organic material at the crystallization front and occlusion of organics during crystallization (the latter has been shown in Ref.

[15]). When the crystallization front passes a mineral bridge, this branch of the crystal has a very small diameter and is therefore sensitive to small stresses. The stresses and occlusions will result in small changes of orientation of the lattice and in potential growth faults. Thus small orientation gradients will be present in the association of capsules composing a grain (Fig. 6a and b).

The jigsaw structure develops as follows: simultaneously active crystallization pathways originating from different nucleation centres will form neighbouring grains of different orientation (Fig. 6c and d). Depending on the random connectivity of the ACC capsules, simultaneously growing calcite crystallites will form interlocking nano- to microstructures (Fig. 6c and d). A second mechanism may even be more important: as crystallization advances, remnants of vesicle membranes (as observable in Fig. 3b and c) are pushed ahead by the crystallization front and accumulate in thicker films (indicated by the wiggly and black lines in Fig. 6a and c, respectively). These films will eventually obstruct the crystal growth fronts and also generate random boundaries between different crystals of the observed dendritic microstructure of the primary shell layer that is sketched in Fig. 6d.

5. Concluding summary

1. We found a new distinct type of micro/nanoscale structural architecture of biogenic calcium carbonate material. It consists of interdigitated dendrite-like calcite mesocrystals. We put forward a model of crystallization from an amorphous calcium carbonate precursor containing organic constituents.
2. The mesocrystal dendrites reach sizes of tens of micrometres. However, these grains are strongly interdigitating, resulting in a nanoscale topology of grain boundaries. This gives the extraordinary microhardness of the brachiopod shell primary layer.
3. As in the case of the now well-known types of carbonate shell material architectures – laminar nacre [1], fibrous calcite [12] and calcite seminacre [46] – the biologically controlled mineral nano/microstructure has no correspondence to inorganic carbonate fabrics, and it is highly optimized towards mechanical performance.
4. The preferred crystallographic orientation is quantitatively similar in calcite shell layers with completely different grain morphologies and grain boundary topologies. This indicates a common control mechanism for nucleation, probably from a common ACC precursor, but different modes of growth in the distinct organic matrices of the two layers.
5. We describe four hierarchical levels of structure of brachiopod shell material: nanosized capsules or granules, mesocrystals consisting of capsules, a 3-D jigsaw microstructure in the primary layer and submillimetre scale layering of the shell involving other fibre or columnar architectures [10,12,15] not described here.

Acknowledgements

We are indebted to R. Enders for the sample preparation and A. Logan and K. von Allmen for providing the samples, as well as the Deutsche Forschungsgemeinschaft (DFG) for financial support of the project.

References

- [1] Currey JD. The design of mineralised hard tissues for their mechanical functions. *J Exp Biol* 1999;202:3285–94.
- [2] Miserez A, Weaver JC, Thurner PJ, Aizenberg J, Dauphin Y, Fratzl P, et al. Effects of laminate architecture on fracture resistance of sponge biosilica: lessons from nature. *Adv Funct Mater* 2008;18:1241–8.

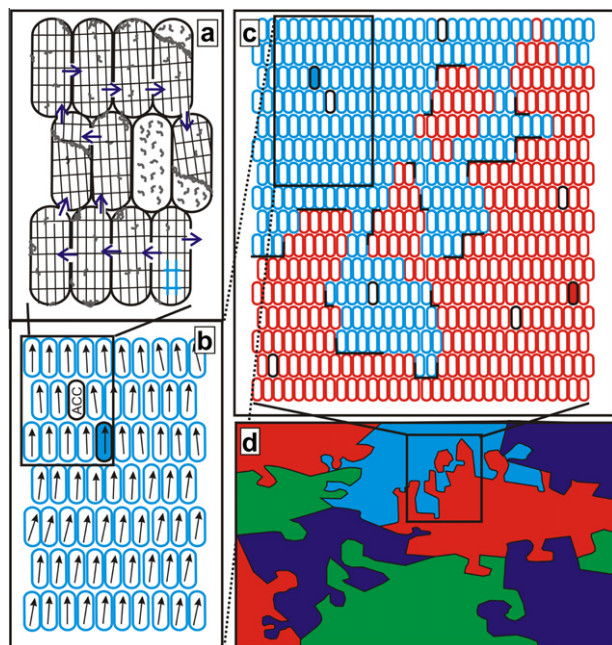


Fig. 6. Schematic model for shell growth with a shell microstructure consisting of splined and interwoven/interdigitating grains. ACC is present in confined capsules that are contoured by vesicle membranes (a). Crystallization takes place within the capsules and at distinct nucleation sites (a, blue lattice; b and c, blue/red filled capsule with black border). Crystallization continues and can proceed due to the presence of mineral bridges between the capsules (a). At the crystallization front, organic macromolecules present in ACC, shown schematically with small black wiggly lines in (a), accumulate. Stress at the mineral bridges leads to a slight crystallographic misorientation between different capsules (a and b). Several capsules form a mesocrystalline grain and lead to the development of in-grain gradients. This non-continuous growth depends on jumps from capsule to capsule and ACC can still be present in single capsules, as indicated by the black, empty capsules in (b and c). The accumulation of organic macromolecules (black lines in c) during crystallization can stop the growth of a crystal in one direction entirely and will lead to the observed microstructure of the primary shell layer (d).

- [3] Tai K, Dao M, Suresh S, Palazoglu A, Ortiz C. Nanoscale heterogeneity promotes energy dissipation in bone. *Nat Mater* 2007;6:454–62.
- [4] Currey JD. Materials science – hierarchies in biomineral structures. *Science* 2005;309:253–4.
- [5] Okumura K, de Gennes PG. Why is nacre strong? Elastic theory and fracture mechanics for biocomposites with stratified structures. *Eur Phys J E* 2001;4:121–7.
- [6] Rousseau M, Lopez E, Stempfle P, Brendle M, Franke L, Guette A, et al. Multiscale structure of sheet nacre. *Biomaterials* 2005;26:6254–62.
- [7] Rudwick MJS. The growth and form of brachiopod shells. *Geol Mag* 1959;96:1–24.
- [8] Williams A, Cusack M, Mackay S. Collagenous chitinophosphatic shell of the brachiopod *Lingula*. *Philos Trans R Soc B* 1994;346:223–66.
- [9] Williams A, Brunton CHC, Carlson SJ, Alvarez F, Ansell D, Baker G, et al. Treatise on Invertebrate Paleontology, Part H, brachiopoda (revised), vol. 6. Lawrence, KS: Geological Society of America and University Press of Kansas; 2007.
- [10] Goetz AJ, Griesshaber E, Neuser RD, Luter C, Huhner M, Harper E, et al. Calcite morphology, texture and hardness in the distinct layers of rhynchonelliform brachiopod shells. *Eur J Mineral* 2009;21:303–15.
- [11] Griesshaber E, Schmahl WW, Neuser R, Job R, Bluem M, Brand U. Microstructure of brachiopod shells—an inorganic/organic fiber composite with nanocrystalline protective layer. *Mater Res Soc Symp Proc* 2005;851:99–104.
- [12] Griesshaber E, Schmahl WW, Neuser R, Pettke T, Blum M, Mutterlose J, et al. Crystallographic texture and microstructure of terebratulide brachiopod shell calcite: an optimized materials design with hierarchical architecture. *Am Mineral* 2007;92:722–34.
- [13] Merkel C, Griesshaber E, Kelm K, Neuser R, Jordan G, Logan A, et al. Micromechanical properties and structural characterization of modern inarticulated brachiopod shells. *J Geophys Res–Biogeo* 2007;112. Artn G02008.
- [14] Perez-Huerta A, Cusack M, England J. Crystallography and diagenesis in fossil craniid brachiopods. *Palaeontology* 2007;50:757–63.
- [15] Schmahl WW, Griesshaber E, Merkel C, Kelm K, Deuschle J, Neuser RD, et al. Hierarchical fibre composite structure and micromechanical properties of phosphatic and calcitic brachiopod shell biomaterials – an overview. *Mineral Mag* 2008;72:541–62.
- [16] Schmahl WW, Griesshaber E, Neuser R, Lenze A, Job R, Brand U. The microstructure of the fibrous layer of terebratulide brachiopod shell calcite. *Eur J Mineral* 2004;16:693–7.
- [17] Griesshaber E, Kelm K, Sehrbrock A, Job R, Schmahl WW, Mader W. The ultrastructure of brachiopod shells: a mechanically optimized material with hierarchical architecture. In: Bushby AJ, Ferguson VL, Ko CC, Oye ML, editors. *Mechanical Behavior of Biological and Biomimetic Materials*. Warrendale, PA: Materials Research Society; 2006.
- [18] Kamat S, Su X, Ballarini R, Heuer AH. Structural basis for the fracture toughness of the shell of the conch *Strombus gigas*. *Nature* 2000;405:1036–40.
- [19] Schmahl WW, Kelm K, Griesshaber E, Goetz A, Jordan G, Xu D, et al. The hierarchical organization in biomaterials: from nanoparticles via mesocrystals to functionality. *Semin Soc Esp Mineral* 2010;07:5–21.
- [20] Ji BH, Gao HJ, Hsia KJ. How do slender mineral crystals resist buckling in biological materials? *Philos Mag Lett* 2004;84:631–41.
- [21] Mayer G. New classes of tough composite materials – lessons from natural rigid biological systems. *Mat Sci Eng C–Bio S* 2006;26:1261–8.
- [22] Griesshaber E, Neuser R, Schmahl WW. The application of EBSD analyses to biomaterials: microstructural and crystallographic texture variations in marina carbonate shells. *Semin Soc Esp Mineral* 2010;07:22–34.
- [23] Griesshaber E, Kelm K, Sehrbrock A, Mader W, Mutterlose J, Brand U, et al. Amorphous calcium carbonate in the shell material of the brachiopod *Megerlia truncata*. *Eur J Mineral* 2009;21:715–23.
- [24] Addadi L, Raz S, Weiner S. Taking advantage of disorder: amorphous calcium carbonate and its roles in biomineralization. *Adv Mater* 2003;15:959–70.
- [25] Beniaeh E, Aizenberg J, Addadi L, Weiner S. Amorphous calcium carbonate transforms into calcite during sea urchin larval spicule growth. *P Roy Soc Lond B Bio* 1997;264:461–5.
- [26] Weiss IM, Tuross N, Addadi L, Weiner S. Mollusc larval shell formation: amorphous calcium carbonate is a precursor phase for aragonite. *J Exp Zool* 2002;293:478–91.
- [27] Merkel C, Deuschle J, Griesshaber E, Enders S, Steinhauser E, Hochleitner R, et al. Mechanical properties of modern calcite – (*Mergerlia truncata*) and phosphate-shelled brachiopods (*Discradisca stella* and *Lingula anatina*) determined by nanoindentation. *J Struct Biol* 2009;168:396–408.
- [28] Schmahl WW, Griesshaber E, Neuser RD, Goetz A, Luter C. Electron backscatter diffraction study of brachiopod shell calcite – microscale phase and texture analysis of a polycrystalline biomaterial. *Part Part Syst Char* 2009;25:474–8.
- [29] Steinmetz DR, Zaefferer S. Towards ultrahigh resolution EBSD by low accelerating voltage. *Mat Sci Tech* 2010;26:640–5.
- [30] Ren SX, Kenik EA, Alexander KB, Goyal A. Exploring spatial resolution in electron back-scattered diffraction experiments via Monte Carlo simulation. *Microsc Microanal* 1998;4:15–22.
- [31] von Allmen K, Nagler TF, Pettke T, Hippler D, Griesshaber E, Logan A, et al. Stable isotope profiles (Ca, O, C) through modern brachiopod shells of *T. Septentrionalis* and *G. vitreus*: implications for calcium isotope paleo-ocean chemistry. *Chem Geol* 2010;269:210–9.
- [32] Wright SI, Nowell MM. EBSD image quality mapping. *Microsc Microanal* 2006;12:72–84.
- [33] Goldstein JI, Newbury DE, Echlin P, Joy DC, Romig AD, Lyman CE, et al. *Scanning Electron Microscopy and X-Ray Microanalyses*. 2nd ed. New York: Plenum Press; 1992.
- [34] Meldrum FC, Colfen H. Controlling mineral morphologies and structures in biological and synthetic systems. *Chem Rev* 2008;108:4332–432.
- [35] Vielzeuf D, Floquet N, Chatain D, Bonnet F, Ferry D, Garrabou J, et al. Multilevel modular mesocrystalline organization in red coral. *Am Mineral* 2010;95:242–8.
- [36] Vielzeuf D, Garrabou J, Baronnet A, Grauby O, Marschal C. Nano to macroscale biomineral architecture of red coral (*Corallium rubrum*). *Am Mineral* 2008;93:1799–815.
- [37] Asta M, Beckermann C, Karma A, Kurz W, Napolitano R, Plapp M, et al. Solidification microstructures and solid-state parallels: recent developments, future directions. *Acta Mater* 2009;57:941–71.
- [38] Eiken J. Dendritic growth texture evolution in Mg-based alloys investigated by phase-field simulation. *Int J Cast Metal Res* 2009;22:86–9.
- [39] Lasagni F, Lasagni A, Holzappel C, Mucklich F, Degischer HP. Three dimensional characterization of unmodified and Sr-modified Al–Si eutectics by FIB and FIB EDX tomography. *Adv Eng Mater* 2006;8:719–23.
- [40] Steinbach I. Phase-field models in materials science. *Model Simul Mater Sc* 2009;17. Artn 073001.
- [41] Suzuki K, Sasaki M. Microstructure and mechanical properties of liquid-phase-sintered SiC with AlN and Y2O3 additions. *Ceram Int* 2005;31:749–55.
- [42] Borrero-Lopez O, Ortiz AL, Guiberteau F, Padture NP. Improved sliding-wear resistance in in situ-toughened silicon carbide. *J Am Ceram Soc* 2005;88:3531–4.
- [43] Williams A. Evolution of the shell structure of articulate brachiopods. *Spec Pap Palaeontol* 1968:1–55.
- [44] Jacob DE, Soldati AL, Wirth R, Huth J, Wehrmeister U, Hofmeister W. Nanostructure, composition and mechanisms of bivalve shell growth. *Geochim Cosmochim Acta* 2008;72:5401–15.
- [45] Schaffer TE, Ionescu-Zanetti C, Proksch R, Fritz M, Walters DA, Almqvist N, et al. Does abalone nacre form by heteroepitaxial nucleation or by growth through mineral bridges? *Chem Mater* 1997;9:1731–40.
- [46] England J, Cusack M, Dalbeck P, Perez-Huerta A. Comparison of the crystallographic structure of semi nacre and nacre by electron backscatter diffraction. *Cryst Growth Des* 2007;7:307–10.